Draft version October 9, 2019
Typeset using LaTeX twocolumn style in AASTeX62

3D Distribution Map of HI Gas and Galaxies Around an Enormous Lyα Nebula and Three QSOs at $z = 2.3$ Revealed by the HI Tomographic Mapping Technique

Shiro Mukae,[1,2] Masami Ouchi,[1,3] Zheng Cai,[4,5] Khee-Gan Lee,[3] J. Xavier Prochaska,[5,3] Sebastiano Cantalupo,[6] Zheng Zheng,[7] Kentaro Nagamine,[8,9,3] Nao Suzuki,[3] John D. Silverman,[3] Toru Misawa,[10] Akio K. Inoue,[11,12] Joseph F. Hennawi,[13] Yuichi Matsuda,[14,15] Ken Mawatari,[1] Yuma Sugahara,[1,16] Takashi Kojima,[1,16] Yoshiaki Ono,[1] Takatoshi Shibuya,[17] Yuichi Harikane,[14] Seiji Fujimoto,[11] Suzuka Koyamada,[10] Yi-Kuan Chiang,[18] Haibin Zhang,[1,16] and Ryota Kakuma[1,2]

[1] Institute for Cosmic Ray Research, The University of Tokyo, 5-1-5 Kashiwanoha, Kashiwa, Chiba 277-8582, Japan
[2] Department of Astronomy, Graduate School of Science, The University of Tokyo, 7-3-1 Hongo, Bunkyo, Tokyo, 113-0033, Japan
[3] Kavli Institute for the Physics and Mathematics of the Universe (Kavli IPMU, WPI), University of Tokyo, 5-1-5 Kashiwanoha, Kashiwa, Chiba, 277-8583, Japan
[4] Department of Astronomys, Tsinghua University, Beijing 100084, China
[5] UCO/Lick Observatory, University of California, 1156 High Street, Santa Cruz, CA 95064, USA
[6] Department of Physics, ETH Zurich, Wolgang-Pauli-Strasse 27, 8093, Zurich
[7] Department of Physics and Astronomy, University of Utah, 115 South 1400 East #201, Salt Lake City, UT 84112
[8] Department of Earth and Space Science, Graduate School of Science, Osaka University, Toyonaka, Osaka 560-0043, Japan
[9] Department of Physics & Astronomy, University of Nevada, Las Vegas, 4505 S. Maryland Pkwy, Las Vegas, NV 89154-4002, USA
[10] School of General Education, Shinshu University, 3-1-1 Asahi, Matsumoto, Nagano 390-8621, Japan
[11] Department of Physics, School of Advanced Science and Engineering, Waseda University, 3-4-1, Okubo, Shinjuku, Tokyo 169-8555, Japan
[12] Waseda Research Institute for Science and Engineering, 3-4-1, Okubo, Shinjuku, Tokyo 169-8555, Japan
[13] Department of Physics, University of California, Santa Barbara, CA 93106, USA
[14] National Astronomical Observatory of Japan, Osawa 2-21-1, Mitaka, Tokyo 181-8588, Japan
[15] Department of Genetics, The Graduate University for Advanced Studies, SOKENDAI, Mishima,411-8540 Japan.
[16] Department of Physics, Graduate School of Science, The University of Tokyo, 7-3-1 Hongo, Bunkyo, Tokyo, 113-0033, Japan
[17] Kitami Institute of Technology, 165 Koen-cho, Kitami, Hokkaido 090-8507, Japan
[18] Department of Physics & Astronomy, Johns Hopkins University, 3400 N. Charles Street, Baltimore, MD 21218, USA

Submitted to ApJ

ABSTRACT

We present an IGM HI tomography map in a survey volume of $16 \times 19 \times 131\ h^{-3}$comoving Mpc^3 (cMpc^3) centered at MAMMOTH-1 nebula and three neighbouring quasars at $z = 2.3$. MAMMOTH-1 nebula is an enormous Lyα nebula (ELAN), hosted by a type-II quasar dubbed MAMMOTH1-QSO, that extends over 1 h^{-1} cMpc with not fully clear physical origin. Here we investigate the HI-gas distribution around MAMMOTH1-QSO with the ELAN and three neighbouring type-I quasars, making the IGM HI tomography map with a spatial resolution of 2.6 h^{-1} cMpc. Our HI tomography map is reconstructed with HI Lyα forest absorption of bright background objects at $z = 2.4-2.9$: one eBOSS quasar and 16 Keck/LRIS galaxy spectra. We estimate the radial profile of HI flux overdensity for MAMMOTH1-QSO, and find that MAMMOTH1-QSO resides in a volume with significantly weak HI absorption. This suggests that MAMMOTH1-QSO has a proximity zone where quasar illuminates and photo-ionizes the surrounding HI gas and suppresses HI absorption, and that the ELAN is probably a photo-ionized cloud embedded in the cosmic web. The HI radial profile of MAMMOTH1-QSO is very similar to those of three neighbouring type-I quasars at $z = 2.3$, which is compatible with the AGN unification model. We compare the distributions of the HI absorption and star-forming galaxies in our survey volume, and identify a spatial offset between density peaks of star-forming galaxies and HI gas. This segregation may suggest anisotropic UV background radiation created by star-forming galaxy density fluctuations.

mukae@icrr.u-tokyo.ac.jp

Keywords: galaxies: formation — intergalactic medium — large-scale structure of universe

1. INTRODUCTION

In the standard picture of the galaxy formation, galaxies form and evolve in the filamentary large-scale structures (LSSs) of both the dark and baryonic matter (e.g., Rauch 1998; Mo et al. 2010). These structures, which we call "cosmic web", play the role of large gas reservoirs for fueling the star formation of galaxies (e.g., Dekel et al. 2009; Fox & Davè 2017; Umehata et al. 2019). The site where baryonic processes between galaxy and intergalactic medium (IGM) take place is manifested in the form of extended Lyα nebula (e.g., Cantalupo 2017; Matsuda et al. 2004; Steidel et al. 2000). The Lyα size of this extended source is also related to the growth of host dark matter halos (Momose et al. 2019).

Enormous Lyα Nebula (ELAN) is extremely extended Lyα nebula discovered around $z \sim 2$ radio-quiet quasars (e.g., Cantalupo et al. 2014; Kikuta et al. 2019). Since the Lyα emission extends > 300 physical kpc (pkpc) beyond virial diameter of host quasar ($\sim$ 280 pkpc), the origin of ELAN is predicted to be quasar photoionization of neutral hydrogen (HI) gas embedded in the cosmic web (e.g., Cantalupo et al. 2012). However, it is not observationally confirmed whether ELAN resides in HI LSSs. IGM HI distribution around ELAN's host quasar is not well explored.

To investigate IGM HI distribution, one can use HI Lyα absorption found in background quasar spectra (e.g., Rauch 1998; Adelberger et al. 2003; Mukae et al. 2017). However, background quasars are rare and their sightlines are too sparse to sample the HI-gas distribution around ELAN. Hennawi et al. (2015) present a study of HI Lyα absorption around an ELAN which resides in an Lyα emitter (LAE) overdensity. Hennawi et al. (2015) use a background quasar with an impact parameter of 100 pkpc from the host quasars, and find a strong HI absorption in the background quasar spectra. However, HI distribution around the ELAN could not be probed with the single background quasar.

Recently, Cai et al. (2017a) discover an ELAN of MAMMOTH-1 nebula in an LAE overdensity that is dubbed BOSS1441 field (Cai et al. 2017b). In the study of Cai et al. (2017a), the narrow-band NB403 imaging with KPNO-4 m/MOSAIC reveals that the MAMMOTH-1 nebula has extremely extended Lyα emission with $\sim$ 440 pkpc (1 h^{-1} cMpc) which could be powered by a host obscured quasar at $z = 2.32$ (Arrigoni Battaia et al. 2018). The BOSS1441 field is originally found by coherently strong intergalactic Lyα absorption systems (CoSLAs) encoded in six background quasar spectra in the Mapping the Most Massive Overdensities through Hydrogen (MAMMOTH) survey (Cai et al. 2016). These background quasars sample the HI distribution around the ELAN on large scales of $\sim 10\ h^{-1}$ comoving Mpc (cMpc), but it is yet unknown the coherent HI overdensity holds on a smaller scales of $\sim 2-3\ h^{-1}$ cMpc around the MAMMOTH-1 nebula.

Small-scale HI-gas distribution around $z \sim 2$ quasars are well studied by the statistical sample of foreground/background quasar pairs in the Quasar Probing Quasar (QPQ) survey (e.g., Prochaska et al. 2013; Lau et al. 2016). They reveal HI absorption enhancement from 100 pkpc to 1 physical Mpc (pMpc) transverse to quasars. Since ELAN is very rare source and found in galaxy overdensity, whether HI distribution around ELAN follows a common trend is unknown.

For probing IGM HI distribution from large to small scales, bright star-forming galaxies can be used as background sources whose sightline density is higher than that of quasars (Lee et al. 2014a; Steidel et al. 2010). Multiple sightlines of background galaxies spatially probe HI LSSs (e.g., Cucciati et al. 2014; Mawatari et al. 2017; Hayashino et al. 2019). Remarkably, Lee et al. (2014a,b) have established a unique technique, called HI tomography, to reconstruct three dimensional (3D) HI gas distribution at $z \sim 2.2-2.5$ with HI Lyα forest absorption found in multiple sightlines of background galaxies. The pilot HI tomography by Lee et al. (2014b) and their successive studies (Lee et al. 2016, 2018) successfully reveal HI LSSs with a spatial resolution of $\sim 2-3\ h^{-1}$ cMpc as the COSMOS Lyα Mapping And Tomography Observations (CLAMATO) survey.

In this study, we investigate the IGM HI distribution around an ELAN by the HI tomography technique for the first time. We carry out the HI tomographic reconstruction around one of the largest ELAN, MAMMOTH-1 nebula, and its host quasar (hereafter MAMMOTH1-QSO) in the BOSS1441 field. Using multiple sightlines of both the bright background galaxies and quasars, we map out the HI LSSs around the ELAN in the extreme LAE overdensity with a spatial resolution of $\sim 2.6\ h^{-1}$ cMpc. Our study of small-scale 3D HI gas distribution is complementary to the MAMMOTH survey that traces HI overdensities on very large scales.

This paper is organized as follows. In Section 2, we describe our sample of background quasars and our target of background galaxies. In Section 3, the details of our observation and spectra are presented. We describe our spectral analysis and HI tomography in Section 4. We present results and discussions in Section 5. Finally, we summarize our findings in Section 6.

Throughout this paper, we use a cosmological parameter set $(\Omega_m, \Omega_\Lambda, \Omega_b, \sigma_8, h)$=$(0.26, 0.74, 0.045, 0.82, 0.70)$ consistent with the nine-year *WMAP* result (Hinshaw et al. 2013). We refer to kpc and Mpc in physical (comoving) units as pkpc and pMpc (ckpc and cMpc), respectively. All magnitudes are in AB magnitudes (Oke & Gunn 1983).

2. DATA AND TARGET

2.1. *Background Quasar Sample*

To explore Hi Lyα absorption at $z = 2.32$, we use spectra of background quasars with a redshift range of $z = 2.4-2.9$. This redshift range is chosen to investigate Hi Lyα absorption in the Lyα forest wavelength range in the rest frame spectra of background quasars. We adopt the Lyα forest wavelength range of $1041-1185$ Å (e,g., Mukae et al. 2017) to avoid the contamination of the Lyβ forest absorption lines and stellar/interstellar absorption lines associated with the quasar host galaxies. Since we study the $z = 2.32$ Hi Lyα absorption that corresponds to the wavelength of 4036 Å in the observed frame, we select the background quasar at $z = 2.4-2.9$, whose Lyα forest wavelength range includes the Hi Lyα absorption at $z = 2.32$.

Our background quasar samples are composed of three subsets of background quasars: (i) quasars whose sightlines are in the center of the BOSS1441 field (BQ1), (ii) quasars whose sightlines are in the outskirts of the BOSS1441 field (BQ2), and (iii) quasars on large scales from the BOSS1441 field (BQ3). We define the regions of (BQ1, BQ2, BQ3) as rectangles where transverse separations from MAMMOTH1-QSO (Table 1) within ΔRA $= (\simeq +0^\circ.1$ and $-0^\circ.2$, $\pm0^\circ.4$, $\pm3^\circ.0)$ and ΔDec $= (\simeq +0^\circ.1$ and $-0^\circ.2$, $\pm0^\circ.3$, $\pm3^\circ.0)$, respectively.

Our background quasar samples are taken from the SDSS DR14 Quasar catalog (hereafter DR14Q: Pâris et al. 2018) that includes all quasars identified by the SDSS-IV/eBOSS surveys (Myers et al. 2015). In the BQ1 region, we find two eBOSS background quasars with $g \leq 21$. Limiting the redshift range of $z = 2.4-2.9$, we select one quasar at $z = 2.4-2.9$, removing the other quasar at $z > 2.9$. In the BQ2 region, we find four eBOSS quasars with $g \leq 21$ at $z = 2.4-2.9$. The six quasars found in the BQ1 and BQ2 regions are consistent with the background quasars used in the discovery of the BOSS1441 field by Cai et al. (2017b). In the BQ3 region, a total of 235 eBOSS background quasars at $z = 2.4-2.9$ with $g \leq 22.5$ are found.

Finally, our background quasar samples consist of (1, 4, 235) quasars at $z = 2.4-2.9$ in the regions of (BQ1, BQ2, BQ3), respectively. Figure 1 shows the position of MAMMOTH1-QSO and the distribution of background quasars in the BQ1 and BQ2 regions.

2.2. *Background Galaxy Target*

2.2.1. *Target for Spectroscopy*

We use the spectra of background galaxies to increase background sightline densities for exploiting the Hi Lyα absorption at $z = 2.32$. Our background galaxy targets for optical spectroscopy are selected from a sample of $z = 2.4-2.9$ UV-bright ($V < 24.85$) star-forming galaxies. The sample construction is based on our multi-band imaging data in the BOSS1441 field and is provided in Section 2.2.2. The redshift range of $z = 2.4-2.9$ is adopted in the same manner as our background quasar sample construction in Section 2.1. The brightness limit of $V < 24.85$ is chosen from the observations of Lee et al. (2016) who have carried out Hi tomography with Hi Lyα absorption at $z = 2.2-2.5$ found in the spectra of background galaxies at $z = 2.3-3.0$.

2.2.2. *Target Selection*

Our background galaxy sample is based on optical and near-IR imaging data sets of the Large Binocular Camera (LBC; Pedichini et al. 2003) on the Large Binocular Telescope (LBT) and the Wide Field Camera (WFCAM; Casali et al. 2007) on the United Kingdom Infrared Telescope (UKIRT), respectively. The optical imaging is conducted by Cai et al. (2017b) over $23' \times 23'$ in the BOSS1441 field. The data consist of three bands: U taken by LBC blue and V, i taken by LBC red. The 5σ limiting magnitudes on a $2''.0$ aperture are 26.6, 26.2, and 26.1 mag, respectively. The near-IR imaging is performed by Cai et al. (in prep.) over $14' \times 18'$ in the BOSS1441 field. The data consist of two bands of J and H. The 5σ limiting magnitudes on a $2''.0$ aperture are 23.7 and 23.1 mag, respectively.

We first construct multi-band photometric catalog with our multi-band imaging data of LBT/LBC and UKIRT/WFCAM. To measure the photometry, we match these image PSFs to the WFCAM H-band image PSF whose typical FWHM is the largest among the multi-band images ($0.''9$). Source detection is performed with the version 2.8.6 of SExtractor (Bertin & Arnouts 1996), and the photometry is measured with MAG_APER magnitudes on a $2''.0$ diameter aperture.

We then compute photometric redshifts $z_{\rm photo}$, using our $UViJH$ photometric catalog. We perform the spectral energy distribution (SED) fitting with the public EAZY code (Brammer et al. 2008). The SED templates are produced with the stellar population synthesis model of Bruzual & Charlot (2003). We adopt the Chabrier initial mass function (Chabrier 2003), a constant star formation for 0.1 Gyr, and a fixed metallicity of $Z = 0.2 \times Z_\odot$. We apply the Calzetti dust attenuation (Calzetti et al. 2000) with $E(B-V) = 0.0$, 0.15, 0.30, and 0.45. We also apply attenuation by IGM absorption with a model of Inoue et al. (2014).

Finally, we construct the sample of background galaxies whose 1σ confidence interval of $z_{\rm photo}$ is within the range of $z = 2.4-2.9$ and V-band magnitude is $V < 24.85$. Our background galaxy sample consists of a total of 131 star-forming galaxies in the BQ1 region.

3. OBSERVATIONS AND SPECTRA

3.1. *Background Quasar Spectra*

Spectra of our background quasar samples (Section 2.1) are taken from the eBOSS data (Myers et al. 2015). We obtain reduced eBOSS spectra that cover the wavelength range of 3600-10400 Å, and have the spectral resolution of $R \equiv \lambda/\Delta\lambda \approx 2000$.

We then examine qualities of the background quasar spectra. We select spectra with $\mathrm{S/N}_{\rm Ly\alpha} \geq 2$, where

Table 1. Properties of MAMMOTH1-QSO

Source	R.A. (J2000)	Decl. (J2000)	$z_{\rm spec}$	V (AB)	Ref. [a]
MAMMOTH1-QSO	14 41 24.46[b]	+40 03 09.20[b]	2.319[c]	24.20	C17

[a] C17: Cai et al. (2017a)

[b] Updated coordinates in Keck/KCWI observations of Cai et al. (in prep.)

[c] The redshift uncertainty of $\simeq 400$ km s^{-1} is adopted for the host quasar (Cai et al. 2017a).

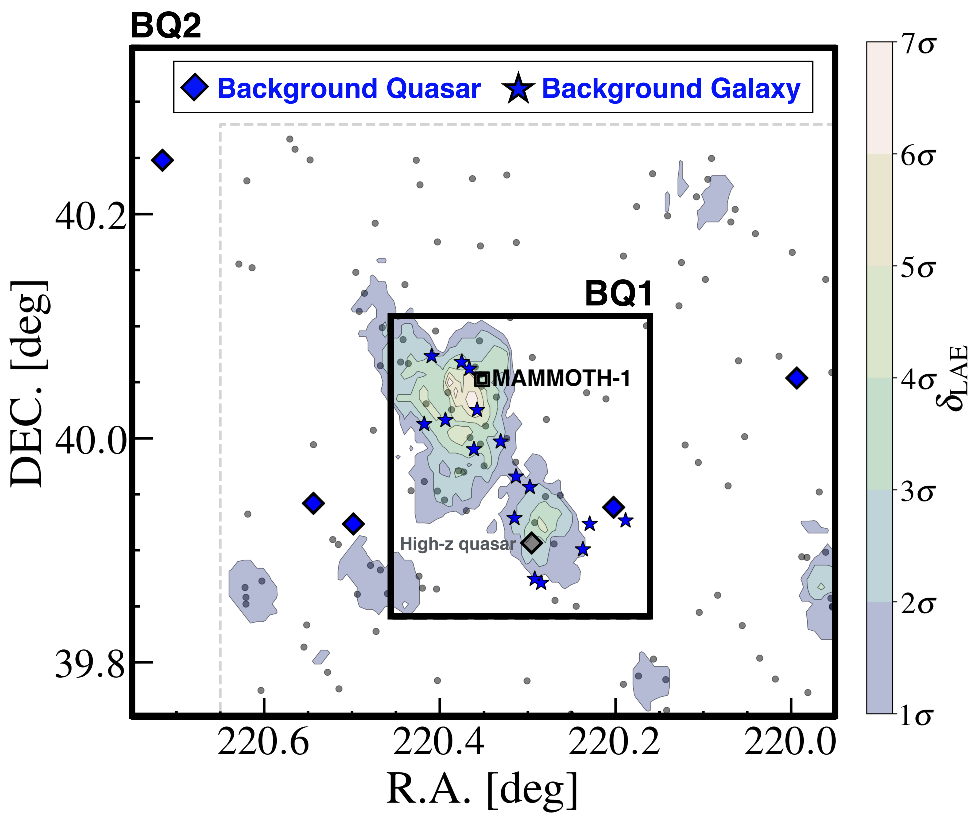

Figure 1. Sky distribution of our background sightlines in the BQ1 and BQ2 regions (Section 2.1). Blue diamonds (stars) represent the position of our background quasars (galaxies) at $z = 2.4 - 2.9$. Gray diamond is a quasar in BQ1 at $z > 2.9$. Double square is the position of MAMMOTH-1 nebula at $z = 2.32$. Dark-gray dots surrounded by the light-gray dashed lines present the distribution of NB403 LAEs in Cai et al. (2017b). Color contour represents $\delta_{\rm LAE}$ measured in Section 5.3.

S/N$_{\rm Ly\alpha}$ is the median signal-to-noise ratio per pixel over the Lyα forest wavelength range (rest frame $1041-1185$ Å). We discard spectra that show broad absorption lines associated with quasar itself by applying BI < 200 km s^{-1} in the DR14Q catalog, where BI (BALnicity Index) is an indicator of trough width seen in the blueward of quasar's C IV emission line. We also remove quasar spectra with damped Lyα systems (DLAs) that contaminate spectra in the Lyα forest wavelength range. We search for DLAs in our quasar spectra mainly based on a DLA catalog of Noterdaeme et al. (2012) and their updated catalog[1] for the SDSS DR12 quasars. We refer to these catalogs by crossmatching our eBOSS background quasars with the SDSS DR12 quasar catalog (Pâris et al. 2017). For spectra of eBOSS quasars who do not have SDSS DR12 counterpart, we perform visual inspection, and remove quasar spectra that have DLAs in the Lyα forest wavelength range. We also check the rest of background quasar spectra by visual inspection, and discard one spectrum with large flux fluctuations

[1] http://www2.iap.fr/users/noterdae/DLA/DLA.html

originated from unknown systematics. Finally, we use background quasar spectra of (1, 4, 109) in the (BQ1, BQ2, BQ3) regions, respectively.

3.2. *Background Galaxy Spectra*

3.2.1. *Keck Spectroscopy*

We select our background galaxy targets for the spectroscopy based on photometric redshift probability, source brightness, and uniformity on the sky. We carried out optical spectroscopy with the Low Resolution Imaging Spectrometer (LRIS) Double-Spectrograph (Oke et al. 1995) on the Keck I telescope on 2017 August 27 (UT) (PI: S. Mukae). We performed the LRIS spectroscopy in the multi-object slit mode using the B600/4000 grism on the blue arm with the d560 dichroic. We chose the slit width of 1".0 that gives a spectroscopic resolution of $R \equiv \lambda/\Delta\lambda \approx 1000$ on the blue arm. The LRIS spectra are covered in the wavelength range of 3800-5500 Å. We observed one mask for the BOSS1441 field with total exposure time of 9000 s in the blue arm. The sky conditions were clear throughout the observing run, with an average seeing size of 0".95.

Our LRIS data on blue channel is reduced with the Low-Redux package [2] in the public XIDL pipeline [3], for long-slit and multi-slit data from the optical spectrographs on the Keck, Gemini, MMT, and Lick telescopes. We extract our LRIS spectra, following the standard reduction procedures. Firstly, the pipeline processes flat with domeflat and twiflat data, calibrates wavelengths with arc data, and rejects cosmic ray injections. Secondly, sources are identified and traced in each slit in individual science frame. Then, sky background subtraction is performed and distortion of two-dimensional (2D) multi-slit mask images are corrected. Next, we extract one-dimensional (1D) spectra of the identified sources from each slit in the individual 2D mask image. Finally, we obtain reduced LRIS spectra by stacking these 1D spectra for each slit of the multiple science frames.

3.2.2. *Keck Archive*

We also take LRIS spectra of background galaxies in the BOSS1441 field from Keck Observatory Archive (KOA) [4]. We obtain the raw data of two LRIS masks taken on 2016 May 9 and 10 (UT) (PI: X. Prochaska) and two LRIS masks taken on 2016 April 5 (UT) (PI: X. Fan) through KOA. The LRIS spectroscopy with these four masks were performed in the multi-object slit mode with the B600/4000 grism on the bluearm and the d560 dichroic. Although the original aim of the spectroscopy with these four masks are to identify rest-frame UV-selected galaxies at $z = 2.3$ in the BOSS1441 field (Cai et al., private communication), the spectra of background galaxies at $z = 2.4 - 2.9$ may be observed in these four masks by chance. We thus reduced these data and obtained LRIS spectra on blue channel in the same manner as our LRIS spectroscopy (see Section 3.2.1), for the purpose of identification of background galaxies at $z = 2.4 - 2.9$.

[2] http://www.ucolick.org/~xavier/LowRedux/
[3] http://www.ucolick.org/~xavier/IDL/
[4] https://www2.keck.hawaii.edu/koa/public/koa.php

4. ANALYSIS

4.1. *Spectroscopic Redshift*

To identify background galaxies at $z = 2.4 - 2.9$, we estimate spectroscopic redshift $z_{\rm spec}$ for the LRIS spectra extracted from our spectroscopic data (Section 3.2.1) and the KOA data (Section 3.2.2). We obtain $z_{\rm spec}$ with the minimum chi-square method in which we perform chi-square fitting of the spectral template of Shapley et al. (2003) to the LRIS spectra. We then identify background galaxies by selecting the spectra of galaxies whose $z_{\rm spec}$ is included in the redshift range of $z = 2.4 - 2.9$. We obtain a total of 20 background galaxy spectra at $z = 2.4 - 2.9$ in the BQ1 field from our spectroscopic data and the KOA data.

4.2. *Intrinsic Continuum*

To probe the HI absorption at $z = 2.32$, we calculate Lyα forest transmission $F(z)$ in the Lyα forest wavelength range for our background galaxies and quasars.

We firstly estimate the intrinsic continua in the Lyα forest wavelength range by applying the MF-PCA continuum fitting technique (Lee et al. 2012). The MF-PCA continuum fitting technique is composed of two steps: (1) applying continuum templates to both the redward and blueward of the Lyα emission line, and (2) adjusting the amplitude and slope of the blueward continuum to the evolution of cosmic mean Lyα forest transmission $F_{\rm cos}(z)$. Here, we use $F_{\rm cos}(z)$ of Faucher-Giguère et al. (2008) and the MF-PCA continuum fitting code of Lee et al. (2013). To robustly estimate the intrinsic continuua, we perform MFPCA continuum fitting for spectra with $\mathrm{S/N_{Ly\alpha}} \geq 2$, removing 3 noisy spectra of background galaxies. In the same manner as Lee et al. (2014b), intrinsic continua of our LRIS galaxy spectra and eBOSS quasar spectra are reproduced with the UV-bright galaxy templates of Berry et al. (2012) and the quasar continuum templates of Suzuki et al. (2005), respectively. There is a possibility that CoSLAs in the BOSS1441 field could bias the estimation of intrinsic continua. We thus mask out the wavelength range of 4036 ± 36Å that corresponds to the redshift range of the BOSS1441 field ($z = 2.32 \pm 0.03$). After conducting our MF-PCA continuum fitting, we include median r.m.s, continuum fitting errors that are (7, 6, 4%) for spectra with the median signal-to-noise ratio over the Lyα forest wavelength range S/N = (< 4, $4 - 10$, > 10) per pixel (Lee et al. 2012). We obtain 17 continuum-estimated spectra for background galaxies and (1, 4, 109) for background quasars in the (BQ1, BQ2, BQ3) regions, respectively.

We then calculate $F(z)$ in the Lyα forest wavelength range by dividing the observed flux by the estimated intrinsic continuum for the spectra of background galaxies and quasars. The Lyα forest transmission error is estimated from pixel noise in the spectra and continuum fitting errors. There is a possibility that the stellar/interstellar absorption associated with the background objects would appear in the Lyα forest wavelength range and bias the results. We mask out the sufficient wavelength width of ± 5 Å around these intrinsic absorption lines of N II $\lambda 1084$ and C III $\lambda 1175$. In our analysis, we do not use spectra where DLAs contaminates the spectra. Quasar spectra with DLAs have been removed from our background quasar sample (Section 3.1). For our background galaxy spectra, we perform visual inspection to search for DLAs, and discard one background galaxy spectrum that might show a damped absorption feature in its Lyα forest wavelength range. Finally, a total of 16 background galaxy spectra are used for our H I tomographic reconstruction. The number of background quasars used for the H I tomography is investigated in the following section.

4.3. *H I Tomographic Reconstruction*

To study H I-gas distribution at $z = 2.32$, we perform H I tomographic reconstruction (e.g., Lee et al. 2014b). Firstly, for each spectrum of our background galaxies and quasars, we calculate the H I flux overdensity δ_F whose negative (zero) value corresponds to the strong (cosmic average) H I Lyα absorption:

$$\delta_F \equiv \frac{F(z)}{F_{\cos}(z)} - 1, \quad (1)$$

where $F_{\cos}(z)$ is cosmic mean Lyα forest transmission measured by Faucher-Giguère et al. (2008):

$$F_{\cos}(z) = \exp[-0.00185(1+z)^{3.92}]. \quad (2)$$

We have confirmed that $F_{\cos}(z)$ at $z \sim 2.3$ is consistent with that estimated with models of Inoue et al. (2014) and Becker et al. (2013) within 2%, which is not as large as the Lyα forest transmission errors.

Figure 2 shows the position of our background galaxies and quasars in the BQ1 region. White shaded region presents the sky coverage of our H I tomographic reconstruction defined by the area within the mean transverse sigtline separation $\langle d_\perp \rangle$ from our background sightlines. Here, we use a total of 17 background sightlines that are 16 galaxies and one quasar at $z = 2.4 - 2.9$ in the BQ1 region (summarized in Table 2). Our background sightlines have $\langle d_\perp \rangle \simeq 2.6\ h^{-1}$ cMpc that is comparable to that of H I tomography map of Lee et al. (2014b). Note that gray shaded region in Figure 2 shows the area where we do not have spectroscopic data of background objects. The sky coverage of our H I tomographic reconstruction has the filling factor of $\simeq 1/2.2$ inside the BQ1 region. We choose the redshift range of $z_{\rm abs} = 2.25 - 2.40$ that sufficiently covers the distribution of H I Lyα absorption within $\sim \pm 65\ h^{-1}$ cMpc from

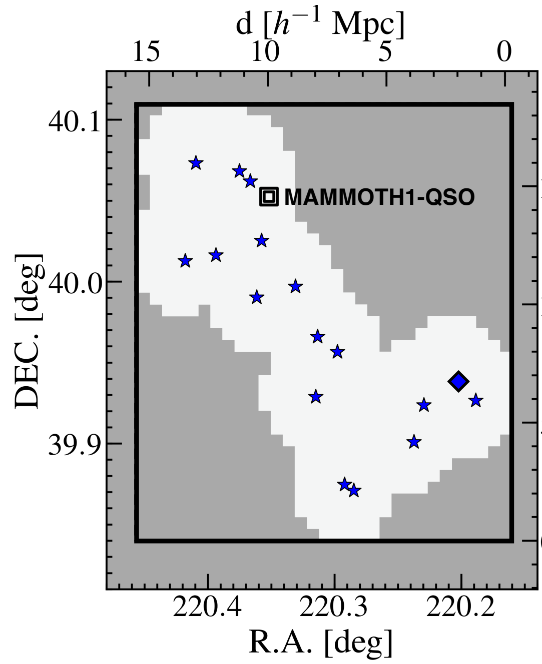

Figure 2. Sky distribution of our background galaxies and quasars in the BQ1 region of the BOSS1441 field. Blue stars (diamonds) represent the position of our background sightlines of galaxies (quasars) at $z = 2.4 - 2.9$. The sky coverage of our H I tomographic reconstruction is shown as the white shaded region defined by the area within the mean transverse sigtline separation $\langle d_\perp \rangle$ from our background sightlines. Double square is the position of MAMMOTH1-QSO at $z = 2.32$. Top and right axes are co-moving separations relative to a corner coordinate (RA, Dec) = (220°.16, 39°.84) of the BQ1 region presented as the black rectangle.

$z_{\rm abs} = 2.32$ in the redshift direction. Our overall survey volume for the H I tomographic reconstruction is defined as the black rectangle (corresponds to the BQ1 region) in Figure 2 across $z_{\rm abs} = 2.25 - 2.40$, which results in $16 \times 19 \times 131\ h^{-3}$cMpc^3.

Finally, we carry out the H I tomographic reconstruction with the code used in Lee et al. (2018) that is developed by Stark et al. (2015) [5]. The reconstruction code performs the Wiener filtering for the H I flux overdensity along our background sightlines in our survey volume. The Wiener filtering is based on the gaussian smoothing with the scale of the mean transverse sightline separation $\langle d_\perp \rangle$. Thus, the spatial resolution of our tomography map is given by $\langle d_\perp \rangle \simeq 2.6\ h^{-1}$ cMpc. In our resulting map, $\langle d_\perp \rangle$ is sampled by 5 pixels of 3D comoving grid with a $(0.5\ h^{-1}\ \text{cMpc})^3$ pixel. More details about the reconstruction process is presented in Lee et al. (2018) and Stark et al. (2015).

[5] https://github.com/caseywstark/dachshund

Table 2. Background objects for Hi tomographic reconstruction

Source	R.A. (J2000)	Decl. (J2000)	$z_{\rm spec}$	g (AB)	V (AB)	Exposure Time (s)	Sample[a]
J144048.56+395618.3	14 40 48.56	+39 56 18.39	2.543	20.04	-	-	eBOSS
20170827_M1_05	14 41 19.44	+39 59 49.52	2.509	-	24.04	7200	LRISs
20170827_M1_07	14 41 26.77	+39 59 25.01	2.816	-	23.40	7200	LRISs
20170827_M1_22	14 41 27.98	+40 03 43.31	2.510	-	24.50	7200	LRISs
20170827_M1_24	14 41 30.05	+40 04 05.59	2.671	-	23.58	7200	LRISs
20160510_M2_05	14 41 11.50	+39 57 24.08	2.546	-	24.11	5400	LRISa
20160510_M2_10	14 41 16.63	+39 58 51.56	2.598	-	23.21	5400	LRISa
20160510_M2_25	14 41 34.49	+40 00 58.68	2.795	-	23.61	5400	LRISa
20160509_M1_11	14 41 40.29	+40 00 46.08	2.557	-	23.05	4000	LRISa
20160509_M1_23	14 41 38.31	+40 04 23.49	2.786	-	22.84	4000	LRISa
20160405_M1_05	14 41 25.85	+40 01 31.40	2.795	-	22.82	6000	LRISa
20160405_M2_08	14 41 10.15	+39 52 28.88	2.791	-	24.27	6000	LRISa
20160405_M2_10	14 41 15.62	+39 55 43.97	2.512	-	24.42	6000	LRISa
20160405_M2_11	14 41 08.38	+39 52 15.59	2.497	-	23.68	6000	LRISa
20160405_M2_20	14 40 56.98	+39 54 03.24	2.703	-	24.34	6000	LRISa
20160405_M2_27	14 40 55.13	+39 55 25.70	2.840	-	24.37	6000	LRISa
20160405_M2_35	14 40 45.31	+39 55 35.76	2.598	-	23.07	6000	LRISa

[a] eBOSS: eBOSS spectroscopy data (Section 3.1),
LRISs: Keck spectroscopy data (Section 3.2.1), LRISa: Keck archive data (Section 3.2.2)

5. RESULTS AND DISCUSSION

5.1. Hi Tomography Map

Figure 3 presents our resulting Hi tomography map made by our background sightlines. We obtain Hi 3D distribution at $z = 2.25 - 2.40$ around MAMMOTH1-QSO for the first time. Our map reveals δ_F values in the range of $+0.4 - (-0.6)$, unveiling Hi overdense ($\delta_F < 0$) and underdense ($\delta_F > 0$) structures. We find Hi overdense ($\delta_F \sim -0.3$) and underdense ($\delta_F \sim 0.3$) LSSs with the size $10 - 20$ h^{-1}cMpc, indicating that Hi gas does not uniformly spread out in the BOSS1441 field.

The error of our Hi tomography map is estimated from the Lyα forest transmission errors of our background sightlines. We generate 1000 data sets of 17 background sightline for which data values include random perturbations following the Gaussian distribution whose sigma is defined by the Lyα forest transmission errors. We obtain 1000 Hi tomographic reconstruction maps, and define the error of our Hi tomography map as the range of 68% distribution for each Hi tomography pixel in the 1000 Hi tomographic reconstruction maps. The 1σ-error of δ_F is 0.08 for each of Hi tomography pixels.

5.2. Hi Radial Profile

5.2.1. Hi gas around MAMMOTH1-QSO

To study the Hi-gas distribution around MAMMOTH1-QSO at $z = 2.32$, we measure the mean radial profile of Hi flux overdensity (hereafter Hi radial profile) around MAMMOTH1-QSO in our Hi tomography map. We calculate the mean δ_F of Hi tomography pixels at 3D distance $R_{\rm 3D}$ from the position of MAMMOTH1-QSO. The 3D distances are computed under the assumption of Hubble flow (zero peculiar velocities of Hi absorbers):

$$R_{\rm 3D} \equiv \sqrt{d_{\rm RA}^2 + d_{\rm Dec}^2 + d_z^2}, \tag{3}$$

where $d_{\rm RA}$, $d_{\rm Dec}$, and d_z are co-moving separations between an Hi tomography pixel and MAMMOTH1-QSO. The error of the mean δ_F is estimated by the random perturbations. We obtain 1000 Hi radial profiles around MAMMOTH1-QSO for the 1000 Hi tomographic reconstruction maps generated in Section 5.1. We define the error of the mean δ_F as the range of 68% distribution for each Hi radial profile in the 1000 data sets.

The black filled circles in Figure 4 presents the Hi radial profile around MAMMOTH1-QSO across ~ 6 pMpc. Note that the scale of $R_{\rm 3D}$ is limited by the

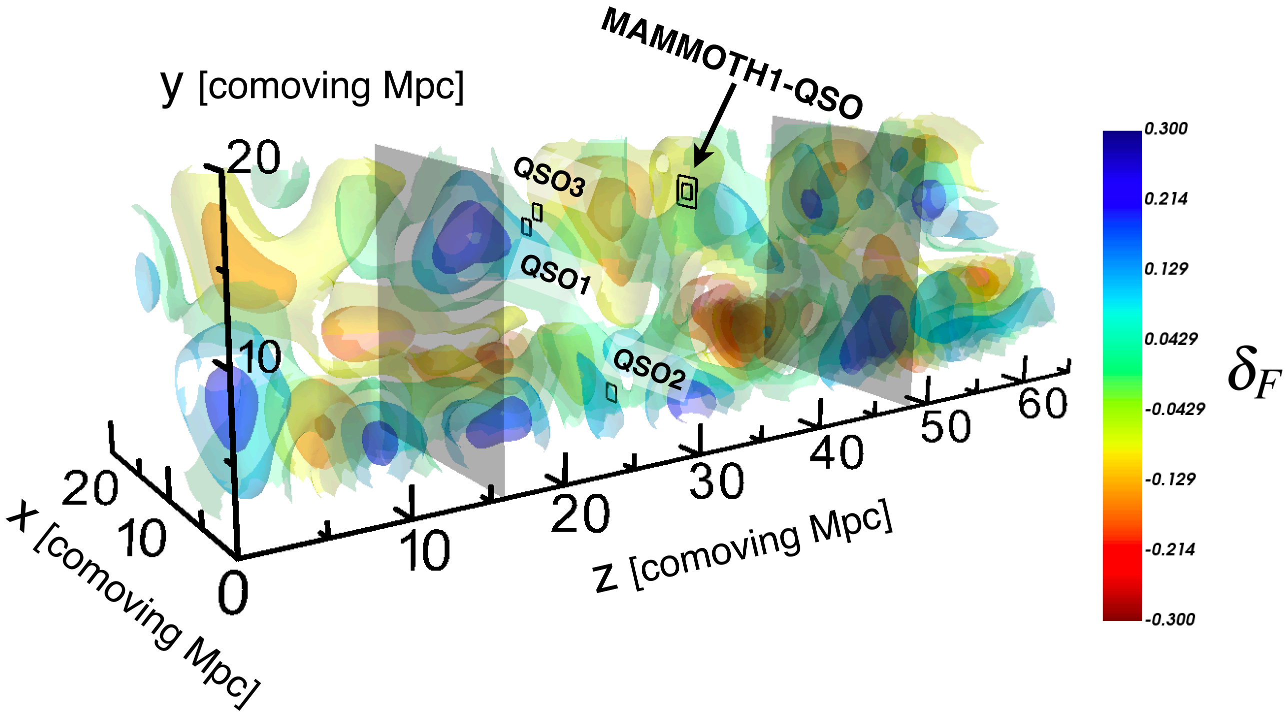

Figure 3. HI tomography map made by our background sightlines. Spatial axes are represented as RA, Dec, z in co-moving scales. Color contours show HI flux overdensity δ_F whose scale range is set to $+0.3$ – (-0.3) for visualization, whereas our map reveals the δ_F values in the range of $+0.4$ – (-0.6). The red color denotes HI overdensities, while blue depicts HI underdensities. Double square indicates the position of MAMMOTH1-QSO. Single squares show the $z \simeq 2.32$ eBOSS quasars (Section 5.2.3). Note that this HI tomography map is a zoomed map at $z = 2.28 - 2.35$ to clarify the redshift range of NB403 (two gray planes) used in Cai et al. (2017a,b), while HI gas distribution is reconstructed across $z = 2.25 - 2.40$.

transverse width of our tomography map. The HI radial profile of MAMMOTH1-QSO shows that HI absorption increases (δ_F decreases) with increasing R_{3D} up to $\simeq 3$ pMpc, from the cosmic average level $\delta_F \simeq 0$ to $\delta_F = -0.06 \pm 0.02$. On the other hand, a marginal increase in δ_F can be seen at $R_{3D} \simeq 3 - 6$ pMpc.

We further investigate the HI radial profile of MAMMOTH1-QSO at $R_{3D} \geq 6$ pMpc beyond our HI tomography map. We use spectra of background quasars at $z = 2.4 - 2.9$ in the BQ2 and BQ3 regions (see Section 2.1) for measurements of the mean δ_F at R_{3D} from MAMMOTH1-QSO. Black open circles in the Figure 4 depict the HI radial profile of MAMMOTH1-QSO beyond our HI tomography map. At $R_{3D} \simeq 10 - 30$ pMpc (based on background quasars in the BQ2 region), the HI radial profile shows enhanced HI absorption consistent with large-scale coherent HI absorption found by Cai et al. (2017b), and connects to the measurements in our HI tomography map. Toward $R_{3D} \simeq 100$ pMpc (based on background quasars in the BQ3 region), HI absorption reaches cosmic average value. Overall, the HI radial profile of MAMMOTH1-QSO across 100 pMpc shows an interesting turnover at $R_{3D} \simeq 3$ pMpc ($\simeq 7\ h^{-1}$ cMpc).

5.2.2. *Comparison with QPQ6*

To investigate our observational results, we compare the HI radial profile around MAMMOTH1-QSO with the results of Prochaska et al. (2013) (hereafter QPQ6) who studied HI radial profiles in the transverse direction around quasars at $z \sim 2$ by a large ensemble of foreground/background quasar pairs. The red filled squares in the Figure 4 represents the mean HI radial profile measured by QPQ6. While the HI radial profile of QPQ6 shows that HI absorption significantly increases with decreasing R_{3D} from $\simeq 1$ pMpc, the HI radial profile of MAMMOTH1-QSO shows the upturn trend with decreasing R_{3D} from $\simeq 3$ pMpc, where HI absorption is much weaker than the QPQ6 results.

The difference between our results and the QPQ6 results suggests that MAMMOTH1-QSO has a proximity zone where quasar illuminates and photo-ionizes the surrounding HI gas and suppresses HI absorption (e.g., D'Odorico et al. 2008; Dall'Aglio et al. 2008). This is because (i) the QPQ6 results are based on type-I AGN that ionizes gas along the line-of-sight direction rather than the transverse direction, while MAMMOTH1-QSO is reported as type-II AGN (Cai et al. 2017a) that ionizes gas along the transverse direction rather than the

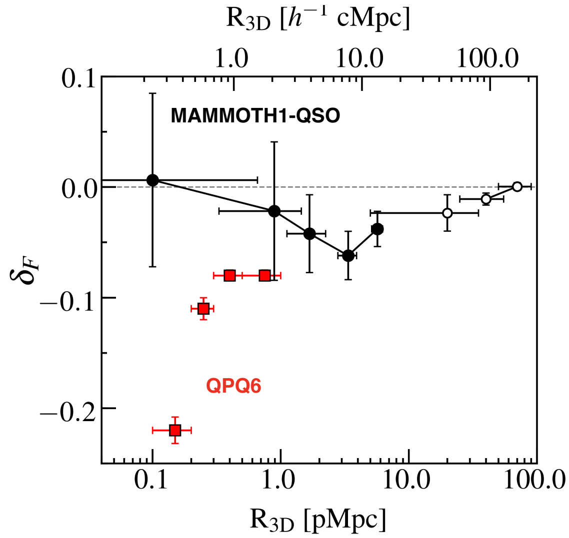

Figure 4. Hi radial profile around MAMMOTH1-QSO as a function of 3D distance R_{3D} from MAMMOTH1-QSO. R_{3D} is computed under the assumption of Hubble flow. Note that the innermost circles show δ_F of the tomography pixel where MAMMOTH1-QSO resides in. Gray dotted line represents the cosmic average value of Hi absorption at $z = 2.32$. The leftmost (right two) open circles show the measurements of background quasars in the BQ2 (BQ3) region. The red squares show the results of QPQ6 (Prochaska et al. 2013).

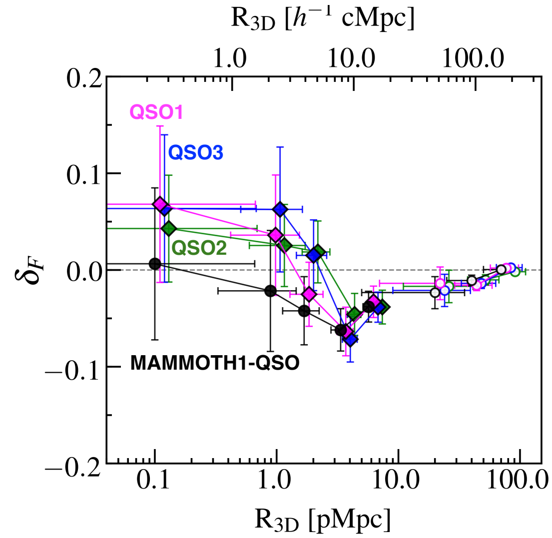

Figure 5. Same as Figure 4, but for Hi radial profiles around $z \simeq 2.32$ quasars in the Hi tomography map. The black, magenta, green, and blue circles represent MAMMOTH1-QSO, QSO1, QSO2, and QSO3, respectively. These circles are slightly offset for clarity.

line-of-sight direction, (ii) QPQ6's Hi radial profile is estimated in the transverse direction, and (iii) our Hi radial profile is estimated with spherical volume that includes the line-of-sight direction as well as the transverse direction.

MAMMOTH1-QSO could be a very bright source along the transverse direction, which likely helps to produce an ELAN of MAMMOTH-1 nebula on the plane of the sky, via photo-ionization of Hi gas on cosmic web.

5.2.3. *Comparison with quasars in Hi tomography map*

We also compare the Hi radial profile around MAMMOTH1-QSO with type-I AGNs in the BOSS1441 field. In the cosmic volume of our Hi tomography map, we find three neighbouring eBOSS quasars at $z \simeq 2.32$ in the DR14Q catalog [6] with the labels of QSO1, QSO2, and QSO3. Note that these eBOSS quasars are regarded as type-I AGN, while MAMMOTH1-QSO is reported as a type-II AGN (Cai et al. 2017a). The coordinates, spectroscopic redshifts and magnitudes of the three eBOSS quasars are summarized in Table 3. Spatial distribution of these quasars are shown in Figure 3.

In the deep NB403 imaging by Cai et al. (2017a,b), no ELAN was detected around QSO1, QSO2, and QSO3. However, there is a possibility that these eBOSS quasars might have extended Lyα nebulae, since the recent high-sensitivity KCWI observations reveal $\sim 100-200$ pkpc Lyα nebulae surrounding bright eBOSS quasars at $z \sim 2$ (Cai et al. 2018, 2019). We use these quasars as a type-I AGN sample with possible Lyα nebulae (but not as large as ELAN). Here, we adopt the spectroscopic redshift of MgII emission line which has small uncertainty of $\simeq 300$ km s^{-1} (Prochaska et al. 2013).

The black magenta, green, and blue circles in the Figure 5 represent the Hi radial profiles of MAMMOTH1-QSO, QSO1, QSO2, and QSO3, respectively. We find the similar trend across 100 pMpc and the common turnover at $R_{3D} \sim 3$ pMpc ($\simeq 7\ h^{-1}$ cMpc) in these four Hi radial profiles, This indicates that type-II AGN has Hi-gas distribution similar to type-I AGN, which is compatible with the AGN unification model (e.g., Antonucci 1993; Elvis 2000).

We visually inspect the Hi-gas distribution around MAMMOTH1-QSO, QSO1, QSO2, and QSO3 in our Hi tomography map. The (X0, X1, X2, X3) panels of Figure 6 show yz slices of our Hi tomography map along x direction with (MAMMOTH1-QSO, QSO1, QSO2, QSO3) at each center. The slice width is comparable to the spatial resolution of our Hi tomography map. We find that there are Hi underdensities with the sizes $\simeq 5-10\ h^{-1}$ cMpc associated with or surrounding MAMMOTH1-QSO, QSO1, QSO2 and QSO3. These sizes are comparable to the proximity zone measurements along the line-of-sight direction at $z \sim 2$ (D'Odorico et al. 2008). This supports the indication of proximity zone around these quasars.

[6] MAMMOTH1-QSO is not observed in the eBOSS survey because of its faintness ($V = 24.20$).

Table 3. $z \simeq 2.32$ eBOSS quasars in the HI tomography map

Source	R.A. (J2000)	Decl. (J2000)	$z_{\rm spec}$	g (AB)	Ref. [a]
QSO1	14 41 33.75	+40 01 42.78	2.306[b]	20.66	DR14Q
QSO2	14 40 49.14	+39 54 07.51	2.306[b]	21.02	DR14Q
QSO3	14 41 21.66	+40 02 58.82	2.305[b]	21.87	DR14Q

[a]DR14Q: Pâris et al. (2018)

[b]Spectroscopic redshift determined by MgII emission line (Pâris et al. 2018). The redshift uncertainty of $\simeq 300$ km s^{-1} is adopted (Prochaska et al. 2013).

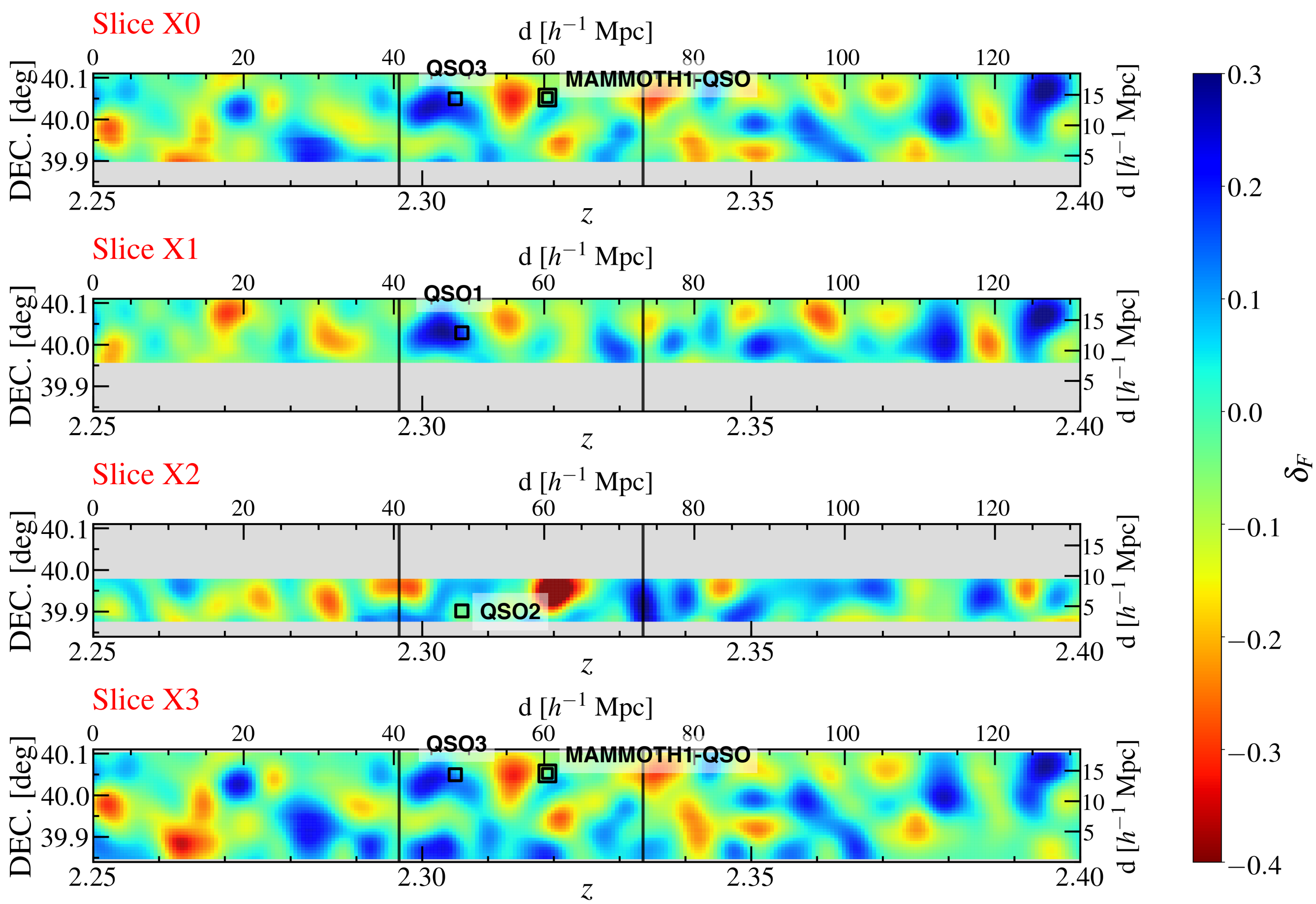

Figure 6. Projecton of HI tomography maps along the x direction. The (X0, X1, X2, X3) panels present yz slices of our HI tomography map along x direction with (MAMMOTH1-QSO, QSO1, QSO2, QSO3) at each center. The slice width is comparable to the spatial resolution of our HI tomography map, and is shown in the red bars in Figure 7. Color scales represent HI flux overdensity δ_F. Double square indicates the position of MAMMOTH1-QSO, while single squares show QSO1, QSO2, and QSO3. Two vertical lines depict the redshift range of NB403 used in Cai et al. (2017a,b).

5.3. *LAE-HI overdensity*

The BOSS 1441 field has a $z = 2.32$ extreme LAE overdensity found in the NB403 imaging by Cai et al. (2017b). To investigate spatial correlations between galaxies and HI gas in the LSSs, we compare the distribution of LAE overdensity with HI gas overdensity in our HI tomography map. Figure 7 shows the sky distribution of LAE overdensity atop the δ_F map at $z = 2.32$.

The δ_F map is calculated by taking average of δ_F of our HI tomography map in z direction across the NB403 redshift range $\Delta z_{\rm NB403}$ ($= 2.30 - 2.33$ corresponding to $\simeq 32.4\ h^{-1}$ cMpc) shown as the volume between the two gray planes in Figure 3.

We compute the LAE overdensity with the LAEs detected in the NB403 imaging of Cai et al. (2017b). The detection limit of these LAEs is Lyα luminosity of $\sim 0.73 L^*_{\rm Ly\alpha}$, where $L^*_{\rm Ly\alpha}$ is the characteristic Lyα luminosity at $z = 2.1 - 3.1$ (Ciardullo et al. 2012). The LAE overdensity $\delta_{\rm LAE}$ is defined as

$$\delta_{\rm LAE} \equiv \frac{n_{\rm LAE}}{\overline{n}_{\rm LAE}} - 1, \tag{4}$$

where $n_{\rm LAE}$ ($\overline{n}_{\rm LAE}$) is the (average) LAE number density in a cylinder. The radius of the cylinder is chosen as $\simeq 2.6\ h^{-1}$ cMpc corresponding to $\langle d_\perp \rangle$ for our tomographic reconstruction. The cylinder length is defined as the NB403 redshift range $\Delta z_{\rm NB4033}$ ($\simeq 32.4\ h^{-1}$ cMpc). The measured LAE overdensity is shown in Figure 1.

In Figure 7, we find two LAE LSSs whose density peaks are at (α=14:41:27.12, δ=+40:02:00.6) and (α =14:41:07840, δ=+39:55:22.8) shown as the purple crosses. These two peaks deviate from HI density peaks by $\sim 3 - 5 h^{-1}$ cMpc, which indicates the spatial offset between density peaks of LAEs and HI gas in LSSs. This segregation between LAE - HI LSSs may reflect anisotropic UV background radiation created by star-forming galaxy density fluctuations inside the BOSS1441 field. Interestingly, the two LAE overdense structures are bridged by one of the HI overdense structures. This implies that the picture that galaxy overdense structures are connected by HI cosmic web.

Note that the segregation between the density peaks of LAEs and HI gas is scale dependent. Cai et al. (2016) investigate signal of correlation between galaxy overdensity and HI overdensity with cosmological simulations (see also Miller et al. 2019). Their simulations suggest that correlation signal is weak in small scale measurements due to geometrical configurations of LSSs. For large scale measurements, Cai et al. (2017b) discover this massive overdensity BOSS1441 field with strong HI absorption systems across $\sim 15\ h^{-1}$ cMpc, and Mukae et al. (2017) find correlation between HI absorption strength and stellar-mass-limited galaxy overdensities around the HI absorption systems with cylindrical volumes whose cubic average scale is $\sim 30\ h^{-1}$ cMpc (see Figure 1 of Cai et al. (2016)).

In Figure 7, the position of MAMMOTH-1 is located on the edge of both density peaks of LAEs and HI gas. This is consistent with results of Lyα nebulae in the overdensity region at $z \sim 2.3$ (Bădescu et al. 2017; Mawatari et al. 2012).

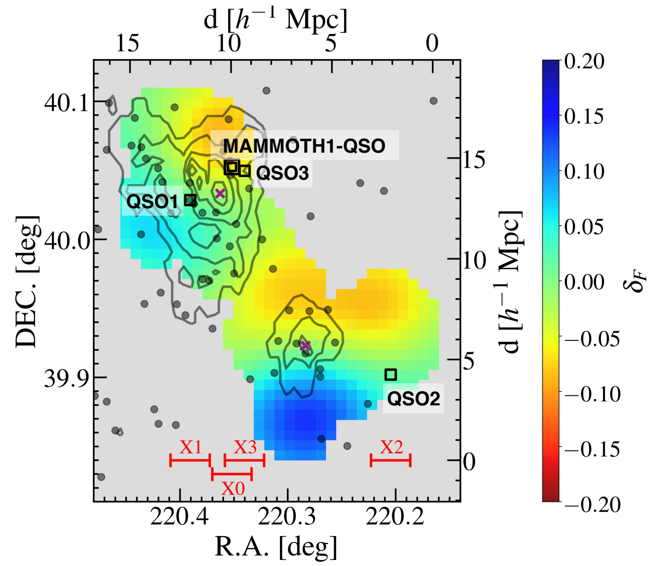

Figure 7. Projecton of HI tomography map across $\Delta z_{\rm NB403}$. Color scales represent δ_F. Gray dots present the distribution of NB403 LAEs of Cai et al. (2017b). Gray contours represent the LAE overdensity excess from 2σ to 6σ. Double square indicates the position of MAMMOTH1-QSO. Single squares show the position of $z = 2.3$ eBOSS quasars. The red bars depict each of the slice width in Figure 6. The purple crosses are the density peaks of the two LAE LSSs.

6. CONCLUSION

We have revealed the 3D distribution of IGM HI gas around an ELAN of MAMMOTH-1 nebula at $z = 2.3$ in a survey volume of $16 \times 19 \times 131\ h^{-3}$cMpc^3 by HI tomography technique with bright background objects at $z = 2.4 - 2.9$ that are one eBOSS quasar and 16 LRIS galaxies. The results of our study are summarized below.

1. The IGM HI tomography map reveals HI overdense ($\delta_F \sim -0.3$) and underdense ($\delta_F \sim 0.3$) LSSs with the size of $10 - 20\ h^{-1}$cMpc, indicating that the diffuse HI gas does not uniformly spread out in the BOSS1441 field.

2. We estimate the HI radial profile spherically averaged around MAMMOTH1-QSO, and identify a turnover at $R_{\rm 3D} \leq 7\ h^{-1}$cMpc where HI absorption is much weaker than the QPQ6 results of the HI radial profile estimated in the transverse to type-I quasars at $z \sim 2$. This suggests that MAMMOTH1-QSO has a proximity zone where quasar illuminates and photo-ionizes

the surrounding H I gas and suppresses H I absorption. MAMMOTH-1 nebula may be originated from photo-ionization of H I gas on cosmic web.

3. We compare the H I radial profile of MAMMOTH1-QSO with those of the three neighbouring eBOSS quasars at $z \simeq 2.32$ found in our H I tomography map. The similarity in these four H I radial profiles estimated with spherical volumes indicate that type-II AGN of MAMMOTH1-QSO has H I-gas distribution similar to type-I AGN, which is compatible with the AGN unification model.

4. We compare distribution of the LAE overdensity with the H I overdensity in our H I tomography map, and identify a spatial offset between density peaks of LAEs and H I gas in LSSs. This spatial offset of LAE - H I LSSs may reflect anisotropic UV background radiation created by star-forming galaxy density fluctuations in the BOSS1441 field.

The connection between IGM H I and galaxy formation in LSSs can be systematically explored by a wide-field spectroscopic survey of the Hobby-Eberly Telescope Dark Energy Experiment (HETDEX: Hill & HETDEX Consortium 2016). The HETDEX survey will provide 10^6 LAEs at $z \sim 2-3$ over 400 deg^2, and reveal a number of extended Lyα nebulae and LSSs such as overdensities and filaments. The LSS/IGM study with HETDEX will be complementary to the ongoing program of CLAMATO (Lee et al. 2018), MAMMOTH (Cai et al. 2016), and the planned program of gigantic IGM tomographic mapping with Subaru/PFS (Nagamine et al. in prep.).

We are grateful to Rieko Momose, Yujin Yang, Satoshi Kikuta, Siddhartha Gurung-Lopez, Marie W. Lau, and Koki Kakiichi for their useful comments and discussions. We also thank Percy Gomez and Nicholas McConnell for their support of our Keck/LRIS observation.

The data presented herein were obtained at the W. M. Keck Observatory, which is operated as a scientific partnership among the California Institute of Technology, the University of California and the National Aeronautics and Space Administration. The Observatory was made possible by the generous financial support of the W. M. Keck Foundation. The authors wish to recognize and acknowledge the very significant cultural role and reverence that the summit of Maunakea has always had within the indigenous Hawaiian community. We are most fortunate to have the opportunity to conduct observations from this mountain. This research has made use of the Keck Observatory Archive (KOA), which is operated by the W. M. Keck Observatory and the NASA Exoplanet Science Institute (NExScI), under contract with the National Aeronautics and Space Administration. Funding for the Sloan Digital Sky Survey IV has been provided by the Alfred P. Sloan Foundation, the U.S. Department of Energy Office of Science, and the Participating Institutions. SDSS-IV acknowledges support and resources from the Center for High-Performance Computing at the University of Utah. The SDSS web site is www.sdss.org. SDSS-IV is managed by the Astrophysical Research Consortium for the Participating Institutions of the SDSS Collaboration including the Brazilian Participation Group, the Carnegie Institution for Science, Carnegie Mellon University, the Chilean Participation Group, the French Participation Group, Harvard-Smithsonian Center for Astrophysics, Instituto de Astrofísica de Canarias, The Johns Hopkins University, Kavli Institute for the Physics and Mathematics of the Universe (IPMU) / University of Tokyo, the Korean Participation Group, Lawrence Berkeley National Laboratory, Leibniz Institut für Astrophysik Potsdam (AIP), Max-Planck-Institut für Astronomie (MPIA Heidelberg), Max-Planck-Institut für Astrophysik (MPA Garching), Max-Planck-Institut für Extraterrestrische Physik (MPE), National Astronomical Observatories of China, New Mexico State University, New York University, University of Notre Dame, Observatário Nacional / MCTI, The Ohio State University, Pennsylvania State University, Shanghai Astronomical Observatory, United Kingdom Participation Group, Universidad Nacional Autónoma de México, University of Arizona, University of Colorado Boulder, University of Oxford, University of Portsmouth, University of Utah, University of Virginia, University of Washington, University of Wisconsin, Vanderbilt University, and Yale University.

This work is supported by World Premier International Research Center Initiative (WPI Initiative), MEXT, Japan, and KAKENHI (15H02064, 17H01110, and 17H01114) Grant-in-Aid for Scientific Research (A) through Japan Society for the Promotion of Science. S.M. acknowledges support from the JSPS through the JSPS Research Fellowship for Young Scientists. S.C. gratefully acknowledges support from Swiss National Science Foundation grant PP00P2_163824. Y.M. acknowledges support from the JSPS grants 17H04831, 17KK0098 and 19H00697.

REFERENCES

Adelberger, K. L., Steidel, C. C., Shapley, A. E., & Pettini, M. 2003, ApJ, 584, 45

Antonucci, R. 1993, ARA&A, 31, 473

Arrigoni Battaia, F., Chen, C.-C., Fumagalli, M., et al. 2018, A&A, 620, A202

Becker, G. D., Hewett, P. C., Worseck, G., & Prochaska, J. X. 2013, MNRAS, 430, 2067

Berry, M., Gawiser, E., Guaita, L., et al. 2012, ApJ, 749, 4

Bertin, E., & Arnouts, S. 1996, A&AS, 117, 393

Brammer, G. B., van Dokkum, P. G., & Coppi, P. 2008, ApJ, 686, 1503
Bruzual, G., & Charlot, S. 2003, MNRAS, 344, 1000
Bădescu, T., Yang, Y., Bertoldi, F., et al. 2017, ApJ, 845, 172
Cai, Z., Fan, X., Peirani, S., et al. 2016, ApJ, 833, 135
Cai, Z., Fan, X., Yang, Y., et al. 2017a, ApJ, 837, 71
Cai, Z., Fan, X., Bian, F., et al. 2017b, ApJ, 839, 131
Cai, Z., Hamden, E., Matuszewski, M., et al. 2018, ApJL, 861, L3
Cai, Z., Cantalupo, S., Prochaska, J. X., et al. 2019, arXiv e-prints, arXiv:1909.11098
Calzetti, D., Armus, L., Bohlin, R. C., et al. 2000, ApJ, 533, 682
Cantalupo, S. 2017, in Astrophysics and Space Science Library, Vol. 430, Gas Accretion onto Galaxies, ed. A. Fox & R. Davé, 195
Cantalupo, S., Arrigoni-Battaia, F., Prochaska, J. X., Hennawi, J. F., & Madau, P. 2014, Nature, 506, 63
Cantalupo, S., Lilly, S. J., & Haehnelt, M. G. 2012, MNRAS, 425, 1992
Casali, M., Adamson, A., Alves de Oliveira, C., et al. 2007, A&A, 467, 777
Chabrier, G. 2003, PASP, 115, 763
Ciardullo, R., Gronwall, C., Wolf, C., et al. 2012, ApJ, 744, 110
Cucciati, O., Zamorani, G., Lemaux, B. C., et al. 2014, A&A, 570, A16
Dall'Aglio, A., Wisotzki, L., & Worseck, G. 2008, A&A, 480, 359
Dekel, A., Birnboim, Y., Engel, G., et al. 2009, Nature, 457, 451
D'Odorico, V., Bruscoli, M., Saitta, F., et al. 2008, MNRAS, 389, 1727
Elvis, M. 2000, ApJ, 545, 63
Faucher-Giguère, C.-A., Prochaska, J. X., Lidz, A., Hernquist, L., & Zaldarriaga, M. 2008, ApJ, 681, 831
Fox, A., & Davè, R. 2017, Gas Accretion onto Galaxies, Vol. 430 (Basel: Springer International Publishing AG), doi:10.1007/978-3-319-52512-9
Hayashino, T., Inoue, A. K., Kousai, K., et al. 2019, MNRAS, 484, 5868
Hennawi, J. F., Prochaska, J. X., Cantalupo, S., & Arrigoni-Battaia, F. 2015, Science, 348, 779
Hill, G. J., & HETDEX Consortium. 2016, in Astronomical Society of the Pacific Conference Series, Vol. 507, Multi-Object Spectroscopy in the Next Decade: Big Questions, Large Surveys, and Wide Fields, ed. I. Skillen, M. Barcells, & S. Trager, 393
Hinshaw, G., Larson, D., Komatsu, E., et al. 2013, ApJS, 208, 19
Inoue, A. K., Shimizu, I., Iwata, I., & Tanaka, M. 2014, MNRAS, 442, 1805
Kikuta, S., Matsuda, Y., Cen, R., et al. 2019, PASJ, 71, L2
Lau, M. W., Prochaska, J. X., & Hennawi, J. F. 2016, ApJS, 226, 25
Lee, K.-G., Hennawi, J. F., White, M., Croft, R. A. C., & Ozbek, M. 2014a, ApJ, 788, 49
Lee, K.-G., Suzuki, N., & Spergel, D. N. 2012, AJ, 143, 51
Lee, K.-G., Bailey, S., Bartsch, L. E., et al. 2013, AJ, 145, 69
Lee, K.-G., Hennawi, J. F., Stark, C., et al. 2014b, ApJL, 795, L12
Lee, K.-G., Hennawi, J. F., White, M., et al. 2016, ApJ, 817, 160
Lee, K.-G., Krolewski, A., White, M., et al. 2018, ApJS, 237, 31
Matsuda, Y., Yamada, T., Hayashino, T., et al. 2004, AJ, 128, 569
Mawatari, K., Yamada, T., Nakamura, Y., Hayashino, T., & Matsuda, Y. 2012, ApJ, 759, 133
Mawatari, K., Inoue, A. K., Yamada, T., et al. 2017, MNRAS, 467, 3951
Miller, J. S. A., Bolton, J. S., & Hatch, N. 2019, arXiv e-prints, arXiv:1909.02513
Mo, H., van den Bosch, F. C., & White, S. 2010, Galaxy Formation and Evolution (Cambridge: Cambridge Univ. Press)
Momose, R., Goto, T., Utsumi, Y., et al. 2019, MNRAS, 488, 120
Mukae, S., Ouchi, M., Kakiichi, K., et al. 2017, ApJ, 835, 281
Myers, A. D., Palanque-Delabrouille, N., Prakash, A., et al. 2015, ApJS, 221, 27
Noterdaeme, P., Petitjean, P., Carithers, W. C., et al. 2012, A&A, 547, L1
Oke, J. B., & Gunn, J. E. 1983, ApJ, 266, 713
Oke, J. B., Cohen, J. G., Carr, M., et al. 1995, PASP, 107, 375
Pâris, I., Petitjean, P., Ross, N. P., et al. 2017, A&A, 597, A79
Pâris, I., Petitjean, P., Aubourg, É., et al. 2018, A&A, 613, A51
Pedichini, F., Giallongo, E., Ragazzoni, R., et al. 2003, in Proc. SPIE, Vol. 4841, Instrument Design and Performance for Optical/Infrared Ground-based Telescopes, ed. M. Iye & A. F. M. Moorwood, 815–826
Prochaska, J. X., Hennawi, J. F., Lee, K.-G., et al. 2013, ApJ, 776, 136
Rauch, M. 1998, ARA&A, 36, 267
Shapley, A. E., Steidel, C. C., Pettini, M., & Adelberger, K. L. 2003, ApJ, 588, 65

Stark, C. W., White, M., Lee, K.-G., & Hennawi, J. F. 2015, MNRAS, 453, 311

Steidel, C. C., Adelberger, K. L., Shapley, A. E., et al. 2000, ApJ, 532, 170

Steidel, C. C., Erb, D. K., Shapley, A. E., et al. 2010, ApJ, 717, 289

Suzuki, N., Tytler, D., Kirkman, D., O'Meara, J. M., & Lubin, D. 2005, ApJ, 618, 592

Umehata, H., Fumagalli, M., Smail, I., et al. 2019, arXiv e-prints, arXiv:1910.01324